applied sciences

MDPI

Article

A Novel Design of Permanent Magnets for the Air Gap Magnetic Field of Hollow-Cup Motor

Jinji Sun, Haoxi Sun and Xueping Xu *

School of Instrumentation and Optoelectronic Engineering, Beihang University, Beijing 100191, China
* Correspondence: xuxueping@buaa.edu.cn

Abstract: Spacecraft motors are often driven with trapezoidal phase currents to achieve higher output torque. For hollow cup motors (HCM) driven by trapezoidal wave currents, parallel magnetised permanent magnet (PM) motors produce an air gap magnetic field (AMF) waveform which is significantly different from the trapezoidal wave, causing the motor to generate noise or vibration. The existing control optimisation method or structure improvement design method is difficult to directly apply to HCM due to its large gas gap. In this paper, according to the fundamental theory of a constant magnetic field, the AMF of HCM is analysed using the equivalent surface current method (ESCM) and its mathematical model is established. The analytical expression of the AMF is solved, and the influencing parameters of the AMF are clarified. The structural design of the HCM with eccentric PMs sintered with high-performance NdFeB is further improved. On this basis, a prototype motor is designed. Simulation results show that the structure can effectively increase the width of the flat section of the AMF and make the AMF close to an ideal trapezoidal wave (ITW). Experiments verify the correctness of the method.

Keywords: eccentric PMs; hollow-cup motor; high-performance NdFeB

Citation: Sun, J.; Sun, H.; Xu, X. A Novel Design of Permanent Magnets for the Air Gap Magnetic Field of Hollow-Cup Motor. *Appl. Sci.* **2023**, *13*, 6537. https://doi.org/10.3390/app13116537

Academic Editor: Gang Lei

Received: 21 March 2023
Revised: 19 May 2023
Accepted: 24 May 2023
Published: 27 May 2023

1. Introduction

As a spacecraft attitude control system, the inertial actuator mainly realises the attitude stabilisation and attitude manoeuvres of the spacecraft. The main principle is to change the angular momentum of the rotor of the high-speed motor and output the control torque. Inertial actuators are mainly divided into magnetically suspended flywheels and magnetically suspended control momentum gyroscopes [1]. As an important part of the space inertial actuator, the drive motor mainly plays the role of controlling or adjusting the rotor speed and then outputting the control torque required to control, adjust, and stabilise the aircraft attitude. For the magnetically suspended flywheel, the attitude control by acceleration and deceleration requires the motor to have higher-speed stabilisation accuracy, smoothness, and lower power consumption. In order to eliminate the iron loss and cogging torque pulsation caused by the presence of the rotor iron core of the conventional DC brushless motor, and to improve the speed accuracy and speed tracking accuracy of the inertia actuator, most inertia actuators use HCM. The main feature of the HCM structure is the use of a rotor without iron core, which overcomes all the problems caused by the iron core, and which greatly improves the main performance of the motor, thus having a wide application field [2]. Due to its superior performance, the HCM has been a hot topic of research in recent years and is used in various fields such as the military, aerospace, automation, industrial robotics, and medical instrument industries [3–6]. In particular, for a magnetically suspended flywheel, it requires the motor to have less torque ripple, thereby improving control accuracy and stability. However, the HCM has a difference between the AMF and the ITW, which causes the back electromotive force (BEMF) waveform to be inconsistent with the ITW, resulting in increased torque ripple and affecting output torque accuracy [7]. At the same time, due to the existence of inter-pole leakage, the pole arc width of the static permanent magnet field is often smaller than the actual pole arc width, causing the stator current to interact with the rotor field, which in turn generates torque fluctuations and causes motor vibration. It is, therefore, necessary to design the structure of the HCM so that the flat section width of the AMF is increased and brought closer to the ITW, further suppressing torque fluctuations and increasing the accuracy of motor torque control. At the same time, due to the extreme temperature difference in the operation of high-speed motors in spacecrafts, the PMs in the motors are susceptible to high-temperature demagnetisation, requiring higher-performance permanent magnet materials.

The torque ripple suppression problem of HCMs is mainly solved by control methods [8–10] or structural design methods [11–14]. Fang et al. [8] proposed an automatic control method based on the measurement of BEMF parameters to adjust the control current with real-time feedback, thus improving the control accuracy and reducing torque pulsation. Zhou et al. [9] proposed a torque prediction analysis based on a neural network fitting analysis incorporating the effects of temperature, with a hybrid braking torque control structure for precise torque control of a small inductance brushless DC motor. In 2017, they [10] adopted the singular perturbation technique to improve the torque tracking performance. For HCMs with a large air gap, it is difficult to reduce the torque pulsation directly through precise control of the winding coil. Regarding the torque ripple caused by nonideal BEMF, from the structural design perspective, the optimisation is mainly carried out by designing the structural design of the PMs or the rotor [11–14]. Zhou et al. [11,12] used the ESCM of PMs to solve the analytical mathematical model of the radial magnetic density generated by the surface-mounted PMs on the stator surface for the brushless DC motor. Through further simulation and experimental analysis of the effect of unequal thickness PMs on the AMF, Ni et al. [13] revised this theory. Kang et al. [14] presented a novel design method for built-in motors. The slot design is performed for the rotor face. The slot positions and the shape parameters of the slots under the optimal solution are obtained using the simulation method, which can effectively reduce the harmonic component of the AMF and increase the flat section width of the AMF. Due to the presence of cogging slots in conventional BLDC motors, it is not possible to eliminate the fluctuations in the AMF caused by the cogging slots, which in turn leads to the generation of cogging torque. For surface-mounted motors, optimising the AMF waveform often starts with designing the PM structure. For built-in PM motors, optimising the AMF waveform often starts with designing the outer diameter of the rotor core to achieve a nonuniform radial air gap thickness; thus, rational optimisation of the PMs structure or the rotor core structure can effectively bring the AMF waveform close to a trapezoidal waveform, which in turn brings the counter-electromotive force waveform close to the ITW, contributing to a suppression of torque pulsation and reduction in motor vibration and noise.

Different structures of motors have different magnetic paths, but the essence of their magnetic paths is the same. In the magnetic circuit, the magnetic lines of force start from the N pole of the PMs, pass through the permeable material and the working air gap, and converge at the S pole of the PMs. In the magnetic circuit, the PMs provide the magnetic momentum, and the magnetic flux passing through the magnetically conductive material generates a magnetic pressure drop. Due to the development of materials science, the relative permeability of various types of magnetically conductive materials is very low, and the magnetic pressure drop generated by the magnetic flux passing through the magnetically conductive material is often very small. The AMF generated by the PMs interacts with the current-carrying coils energised on the cup stator to make the motor work properly. The properties of the permanent magnet material determine the performance of the PMs. Due to the wild temperature variations in the spacecraft operating environment, samarium cobalt alloy materials are often used for PMs in spacecraft in order to avoid high-temperature demagnetisation. Samarium cobalt alloy material has good magnetic properties with a coercivity of up tp 25 MGOe, and a temperature coefficient of less than $-0.037\%/\mathrm{K}$. However, it is not easy to sinter into an eccentric structure, which is difficult to process and costly. Therefore, this paper selects NdFeB materials with high performance and excellent temperature stability. NdFeB materials are widely used in the field of motors due to their excellent electromagnetic properties [15]. The NdFeB permanent magnet easily loses excitation when the working environment of the motor is poor and the iron core loss is large [16,17]. In order to solve this problem, there are two research directions: doping of NdFeB with other rare Earth elements or metal oxides during the sintering and forming process [18–21]. Studies have shown that doping with Ho [18], co-doping with Al/Cu [19], or co-doping with Ga/Cu [20,21] during the sintering and formation of NdFeB PMs can effectively improve the microstructure of the PMs and further enhance their magnetic properties. The magnetic properties of NdFeB materials can also be improved by optimising the NdFeB sintering manufacturing technology [22,23], then changing the bottleneck particle size of the permanent magnet material powder [24]. The improved neodymium iron boron material has a higher service temperature (about 470 K), an extremely high coercivity (35 MGOe), and a relatively excellent temperature coefficient (−0.049%/K).

This paper deals with the HCM using a large air gap. Through the ESCM and Maxwell equations, the analytical solution of the AMF is derived. By improving the structural design of the motor, an eccentric PM sintered with high-performance NdFeB material is designed and manufactured, and the top of the waveform of the AMF becomes flat and close to the ITW, as verified by simulation and experiment.

2. Mathematical Model of AMF

Most high-speed motors in inertial actuators use hollow-cup brushless PM motors. The main feature of the HCM structure is the adoption of the stator coreless structure, which reduces the power consumption of the motor and is widely used in the aerospace field. The main features of HCM are as follows: low rotational inertia, fast starting speed, elimination of the reluctance torque generated by the stator iron core and the eddy current effect caused by losses, thereby improving efficiency, high sensitivity, fast response speed, high power-to-volume ratio, low torque pulsation, low noise, good heat dissipation performance, good phase change performance, long service life, and high reliability.

2.1. HCM Structure

The axial cross-section of the HCM and its plan view are shown in Figure 1. It essentially consists of an inner rotor core (IRC), an outer rotor core (ORC), a variable number of PMs, and a HCM stator. The PMs are made of tile-type magnets which are bonded to the inner diameter of the ORC to prevent the PMs from being thrown off by centrifugal force and to provide a static magnetic field for the motor. The IRC and ORC are made of magnetically conductive material, both of which are fixed to the frame. The winding is wound on the cup stator and placed in the centre of the HCM air gap.

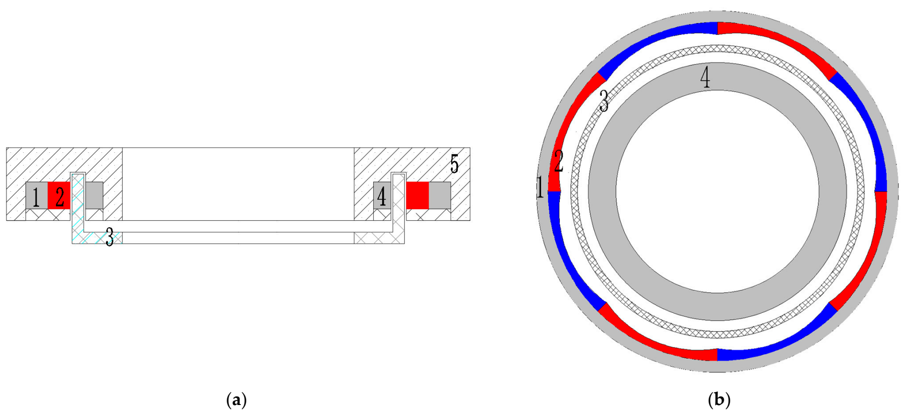

Figure 1. Structure schematic of HCM (1—ORC; 2—PMs: different colours indicate that the adjacent PMs are magnetised in opposite directions; 3—cup stator; 4—IRC; 5—frame): (**a**) axial cross-section view of HCM; (**b**) top view of HCM.

2.2. AMF Analysis Based on ESCM

The AMF of the HCM is generated by PMs. In this paper, the ESCM is used instead of PMs; thus, the magnetic field generated in the air gap of the motor by a current-carrying coil equivalent to PMs is analysed [25,26]. This paper focuses on the analysis of the AMF generated by the parallel magnetised PMs; the end-effects are ignored, and the inner and outer rotor cores are treated as ideal permeable bodies. On the basis of the boundary conditions of the AMF distribution of the HCM, the partial differential equations of the magnetic field distribution of the coil are solved using Maxwell's equation set. The AMF generated by the whole coil can be obtained by applying a superposition of the radial magnetic potential generated on each side of the coil:

$$B(r,\theta) = \frac{\mu_0 i}{\pi r} \sum_{m=1}^{\infty} \frac{R_o^m}{b^m} \left(\frac{R_i^{2m} + b^{2m}}{R_o^{2m} - R_i^{2m}} \right) \left(\frac{r^m}{R_i^m} + \frac{R_i^m}{r^m} \right) \sin(m\alpha)\cos(m\theta), \tag{1}$$

where μ_0 is the air magnetic permeability, α is the angle of the equivalent current coil with respect to the centre line of the PM, η is half the angle of the pair of coils, R_o is the ORC inner diameter, R_i is the IRC outer diameter, (r,θ) denotes the coordinates of any position within the air gap, b is the inner diameter of the PMs, and h_m is the PM thickness.

The correspondence between the PMs and their equivalent currents is shown in Figure 2. When the PMs are magnetised in parallel and there are 2p PMs arranged alternately along opposite magnetisation directions, the superposition of magnetic fields in the air gap by different PMs is

$$Z = \sum_{l=1}^{2p} (-1)^{l-1} \cos m \left[\theta - (l-1)\frac{\pi}{p} \right]. \tag{2}$$

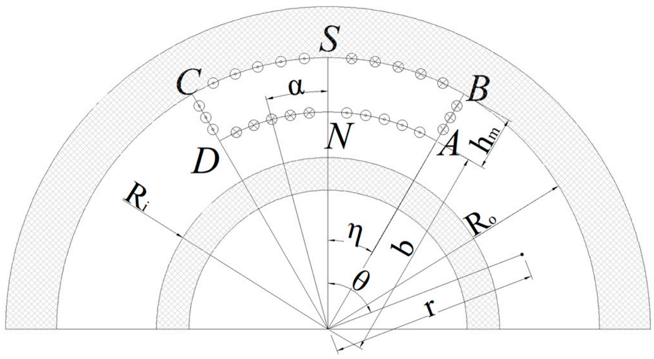

Figure 2. Parallel magnetising tile PMs and the equivalent current coil model.

The remaining coils can be calculated in this way and then superimposed to obtain 2p pairs of the coil sets, producing the following magnetic flux density expression:

$$B(r,\theta) = \frac{\mu_0 i}{\pi r} \sum_{m=1}^{\infty} \frac{R_o^m}{b^m} \left(\frac{R_i^{2m} + b^{2m}}{R_o^{2m} - R_i^{2m}} \right) \left(\frac{r^m}{R_i^m} + \frac{R_i^m}{r^m} \right) \sin(m\alpha) Z. \tag{3}$$

In the ESCM, the equivalent current along the radial side of the PM AB, CD is equal in magnitude and opposite in direction, and the equivalent currents along the AD and BC circumferences sides of the PMs are equal in magnitude and opposite in direction.

Since the AMF is generated by the superposition of several sets of coil currents, the magnetic field distribution must be obtained by integrating the current values on each side. The equivalent current micro-elements di of the AB and CD sides and the AD side are then obtained:

$$\begin{cases} di_{AB-CD} = H_{cb} \cos \eta \, db \\ di_{BC} = H_{cb} \, R_o \sin \alpha \, d\alpha \\ di_{AD} = H_{cb}(R_o - h_m) \sin \alpha \, d\alpha \end{cases}, \tag{4}$$

where H_{cb} is the coercivity, db is the radial length micro-element along the AB and CD sides, and $d\alpha$ is the angular micro-element along the circumferential direction.

According to the above analysis, the motor structure parameters that affect the magnetic field distribution of the motor air gap are the PM thickness h_m, the PM inner diameter b, the ORC inner diameter R_o, the IRC outer diameter R_i, and the motor pole pair number P. Once the structural dimensions and the number of pole pairs of the HCM have been determined, its AMF can be practically changed by the eccentric structure of the PMs.

Figure 3 shows a schematic diagram of the structure after the eccentric transformation of the inner diameter of the PMs. The centre O of the PM inner diameter is moved backwards along the PM centreline to the position of O′. In order to avoid affecting the stator position, the new PM inner diameter has the same position of both end-points, and the new centre of the circle is O′.

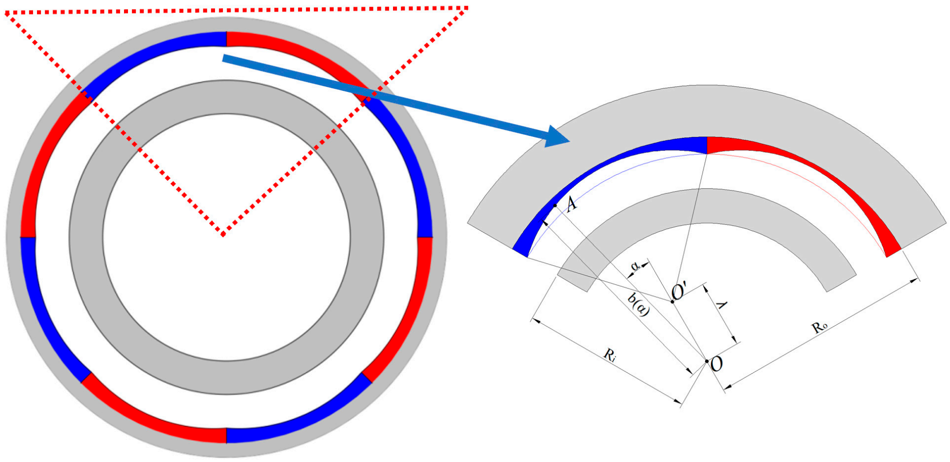

Figure 3. Schematic diagram of the structure of the eccentric PMs of the HCM.

After geometric operations, the coordinates of a point A $(b(\alpha), \alpha')$ on the new inner diameter can be obtained as

$$\begin{cases} b(\alpha) = \sqrt{(R_o - h_m - \lambda)^2 + \lambda^2 - 2\lambda(R_o - h_m - \lambda)\cos(\alpha')} \\ \alpha' = \alpha - \arcsin\frac{\lambda \sin(\alpha)}{R_o - h_m - \lambda} \end{cases}, \tag{5}$$

where λ is the eccentricity of the inner diameter of the PMs, which is the length of the line OO′ in Figure 3.

Substituting Equations (4) and (5) into Equation (3), the micro-element of the AMF strength generated by the equivalent current on each side of the PMs at a point (r, θ) in the air gap after the eccentric optimised design can be obtained as

$$\begin{cases} dB_{AB-CD} = \dfrac{\mu_0 H_{cb} \cos \eta \, db(\alpha)}{\pi r} \sum\limits_{m=1}^{\infty} \dfrac{R_o^m}{b(\alpha)^m} \left(\dfrac{R_i^{2m} + b(\alpha)^{2m}}{R_o^{2m} - R_i^{2m}} \right) \left(\dfrac{r^m}{R_i^m} + \dfrac{R_i^m}{r^m} \right) \sin(m\eta) Z \\ dB_{BC} = \dfrac{\mu_0 H_{cb} R_o \sin \alpha' d\alpha}{\pi r} \sum\limits_{m=1}^{\infty} \left(\dfrac{R_i^{2m} + R_o^{2m}}{R_o^{2m} - R_i^{2m}} \right) \left(\dfrac{r^m}{R_i^m} + \dfrac{R_i^m}{r^m} \right) \sin(m\alpha') Z d\alpha' \\ dB_{AD} = \dfrac{\mu_0 H_{cb} R_o \sin \alpha' d\alpha}{\pi r} \sum\limits_{m=1}^{\infty} \dfrac{R_o^m}{b(\alpha)^m} \left(\dfrac{R_i^{2m} + b(\alpha)^{2m}}{R_o^{2m} - R_i^{2m}} \right) \left(\dfrac{r^m}{R_i^m} + \dfrac{R_i^m}{r^m} \right) \sin(m\alpha') Z d\alpha' \end{cases}. \tag{6}$$

The magnetic field strength at a point (r, θ) in the air gap can be obtained by summing the PM thickness integral along the AB–CD edge and the PM tensor angle integral along the BC and AD edges:

$$B(r,\theta) = \int_{R_o - h_m}^{R_o} dB_{AB-CD} + \int_{-\eta}^{\eta} dB_{BC} + \int_{-\eta}^{\eta} dB_{AD}. \quad (7)$$

The AMF is obtained by solving the above equation along the circumferential direction of the centre line of the air gap in the HCM, and the AMF can be changed by optimising the eccentricity value of the PMs.

3. Finite Element Simulation Verification

In this paper, in order to evaluate the width of flat section of the AMF, the parameter τ is introduced, which is defined as the proportion of the top part to the half waveform width [25], as shown in Figure 4:

$$\tau = \frac{\theta_p}{\alpha_p}, \quad (8)$$

where θ_p is the part of the AMF that lies above 99% of the maximum value B_{max} of the AMF in one cycle, and α_p is the width of the half-cycle of the waveform.

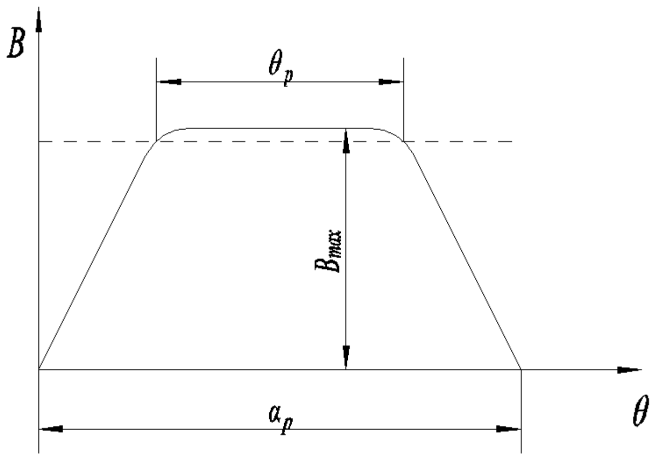

Figure 4. Schematic diagram of the percentage of the flat section of the AMF.

In order to clarify the optimum data of eccentric PMs, the parameters of a four-pole-pair HCM in the laboratory were analysed using the simulation method. The parameters of the HCM are shown in Table 1.

Table 1. Main parameters of the motor.

Item/Unit	Symbol	Parameter
Outer radius of ORC (mm)	R_{o1}	69.2
Inner radius of ORC (mm)	R_o	66
PM thickness (mm)	h_m	3.45
Outer radius of IRC (mm)	R_{i1}	57.3
Inner radius of IRC (mm)	R_i	53
Air gap thickness (mm)	h_{air}	4.55
Pole pairs	p	4
PM remanence (T)	B_r	1.2
PM coercivity (A/m)	H_{cb}	798,000
Magnetising method	-	Parallel magnetisation
ORC and IRC material	-	DT4
PMs material	-	NdFeB N35

A 2D simulation HCM model was constructed using finite element software; the mesh was dissected to appropriate grid elements according to its dimensions using the software mesh dissection tool. The magnetisation characteristic of the motor yoke is shown in Figure 5. The simulation result of the HCM with tile PMs is shown in Figure 6.

The simulation results of the AMF are shown in Figure 7 when the samarium cobalt and NdFeB materials were used for the PMs. It can be seen that the samarium cobalt alloy material was slightly higher than the NdFeB material (by 1.8%), which indicates that the magnetic properties of the two materials were very close to each other.

The AMF was analysed and compared with the waveform calculated using Equation (7), as shown in Figure 8. The analytical result was slightly larger than the simulation result (by 3.4%), but basically consistent, proving the correctness of the above analysis.

The influence of the eccentricity value λ of the inner diameter of the PMs on the AMF waveform was analysed. The results of the AMF waveform under different eccentricity values (tile PMs, 2 mm, 3.5 mm, and 5 mm) are shown in Figure 9. It can be seen that, by adjusting the eccentricity of the inner diameter of the PM sheet, the middle part of the AMF waveform gradually became straight and the wave width gradually increased. Through calculation and simulation verification, when λ was 3.5 mm, the maximum wave width could be obtained. When λ was greater than 3.5 mm, the waveform of the PMs tended to sag, which led to a reduction in the value of τ.

The comparison of AMF under different values λ = 0 and λ = 3.5 mm is shown in Figure 10. In summary, the AMF wave width τ was 32.5% when λ = 0, and τ was 57.8% when λ = 3.5 mm, representing an increase of 77.6%. In other words, adjusting the eccentricity of the inner diameter of the PMs could effectively increase the wave width. The flat section part of the AMF was made straighter, and the wave width ratio was higher, being closer to the trapezoidal shape. In addition, the problems caused by the mismatch between the AMF and the phase current waveform could be effectively reduced.

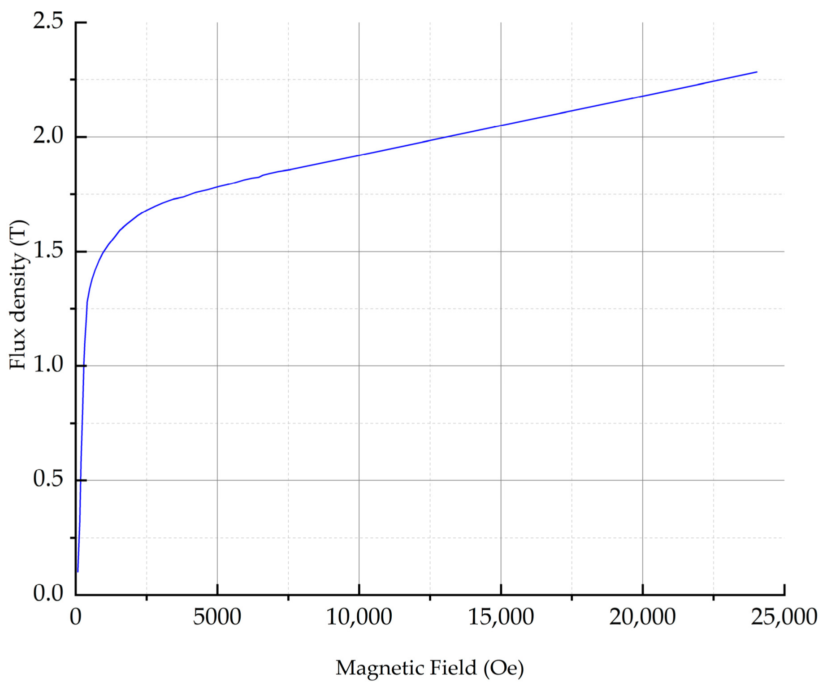

Figure 5. Magnetisation characteristic of the motor yoke.

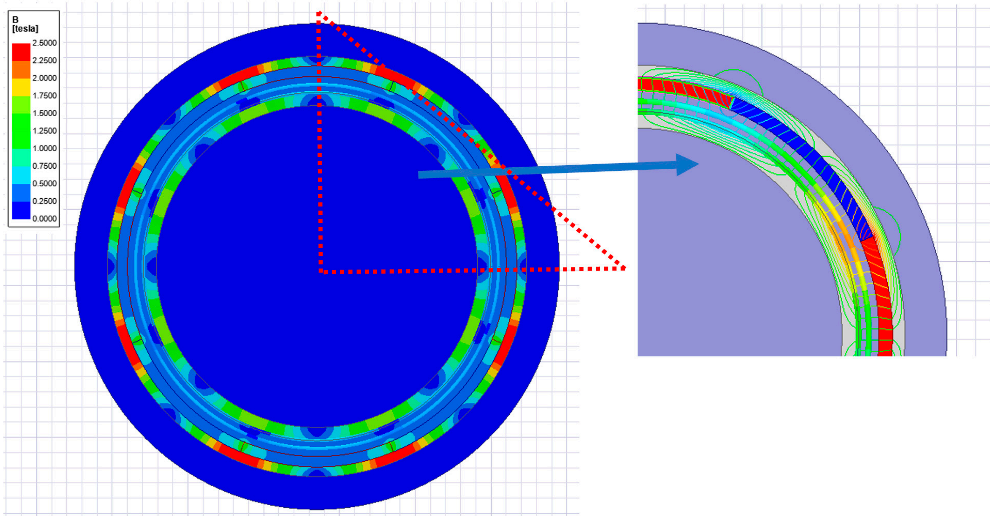

Figure 6. Magnetic field and magnetic line distribution of the HCM with tile PMs.

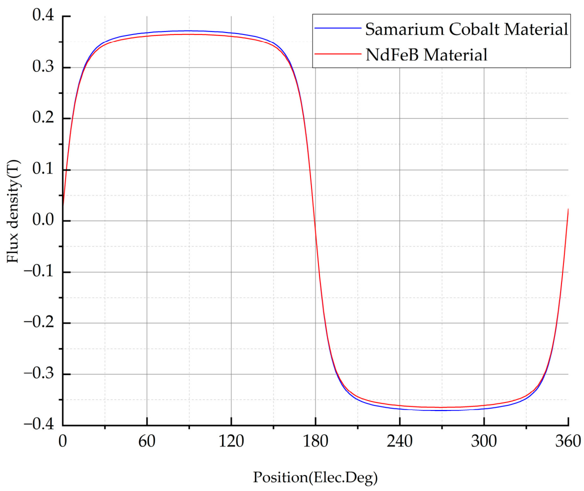

Figure 7. FEA results of samarium cobalt alloy material and NdFeB material.

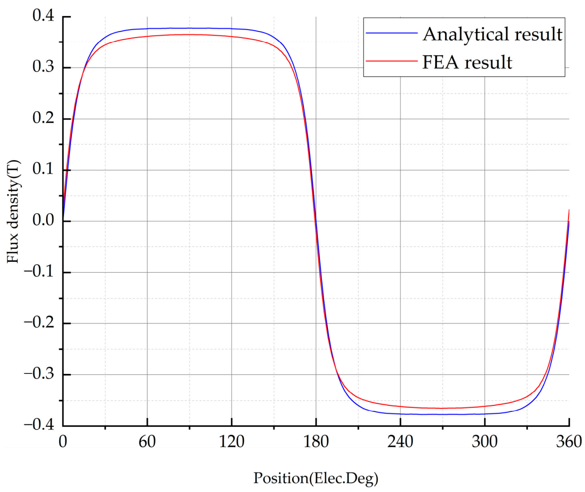

Figure 8. Comparison of analytical result and FEA result.

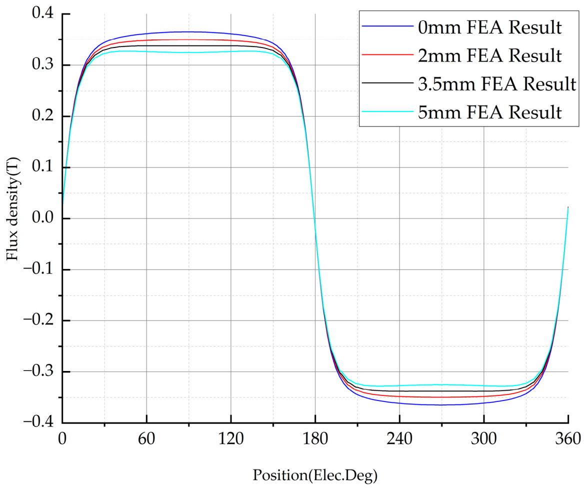

Figure 9. Schematic diagram of the AMF as the eccentricity changes.

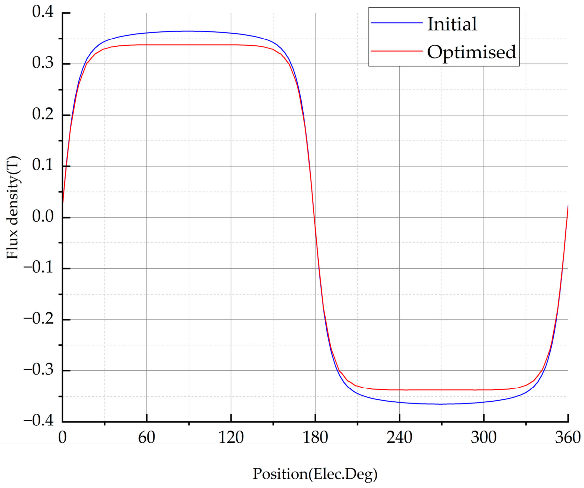

Figure 10. AMF optimisation results.

Analysing the simulation results, we can see that the maximum value of AMF B_{max} was 0.3649 T when the PM was a tile type. When the improvement result was optimal (eccentricity value λ = 3.5 mm), the maximum value of AMF B_{max} was 0.3377 T. B_{max} was reduced by 7.46%; compared with the improvement of τ, the reduction in B_{max} was acceptable.

4. Experimental Verification

In order to clarify the effect of improvement the AMF waveform based on the eccentric design of the PMs and to improve the magnetic properties of the PMs of the motor, two sets of PMs were sintered with high-performance NdFeB permanent magnet materials, tile PMs, and PMs with an eccentricity value of 3.5 mm.

The test prototype was manufactured according to the parameters given in Table 1. The material of the inner and outer rotors was electrically pure iron with a rustproof surface treatment, and the top surface of the inner rotor was scored to ensure that the scores corresponded to the magnetic joints when the prototype was installed to ensure test accuracy. The PMs were made of NdFeB and were designed with different eccentric dimensions according to the simulation results. The inner and outer rotor models and the PM model are shown in Figure 11.

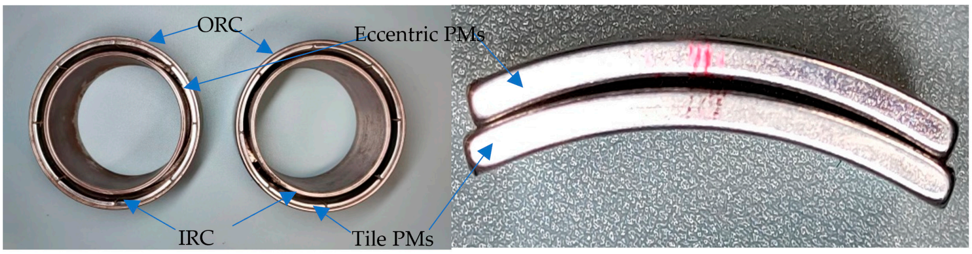

Figure 11. HCM and PM model.

The experimental platform, shown in Figure 12, was mainly composed of the following parts: clamping mechanism, rotary motor, Hall magnetometer, mechanical arm, clamping mechanism consisting of a three-jaw chuck on the centring mechanism, three jaws along the radial movement, connected by thread on the chuck, and adjustable radial position clamping motor model. The rotary motor was firmly connected to the three-jaw chuck and drove the rotation of the three-jaw chuck. The Hall magnetometer measured the strength and direction of the magnetic field at the position of the probe with an accuracy of 0.001 T. The mechanical arm clamped the magnetometer and could adjust its position along the radial direction. After the prototype was assembled and installed on the three-jaw chuck of the experimental platform, the Hall magnetometer was adjusted after clamping and placed at the midpoint of the HCM air gap and the Z- phase of the PMs. The rotary motor drove the prototype to rotate 360° to measure the AMF of two sets of PMs.

Figure 12. AMF test experimental platform.

The FEA result and the experimental result of the PMs under the eccentricity values of 0 mm and 3.5 mm are shown in Figure 13 and Table 2. For the HCM prototype composed of tile-shaped PMs (with an eccentricity value of 0 mm), the values of B_{max} and τ were 0.3649 T and 32.5%, respectively, in the simulation results and 0.3631 T and 29.4%, respectively, in the experimental results, with errors between the experimental and simulation results of 0.48% and 9.54%, respectively. For the HCM prototype composed of the PMs with an eccentricity value of 3.5 mm, the values of B_{max} and τ were 0.3377 T and 57.8%, respectively, in the simulation result and 0.3362 T and 56.3%, respectively, in the experimental result, with errors between the experimental and simulation results of 0.44% and 2.60%, respectively. The experimental result was in general agreement with the simulation result, further confirming the correctness of the theory. This further illustrates that, in the case of parallel magnetisation of the PMs, the AMF of the motor could be changed to the required waveform by changing the shape of the PMs.

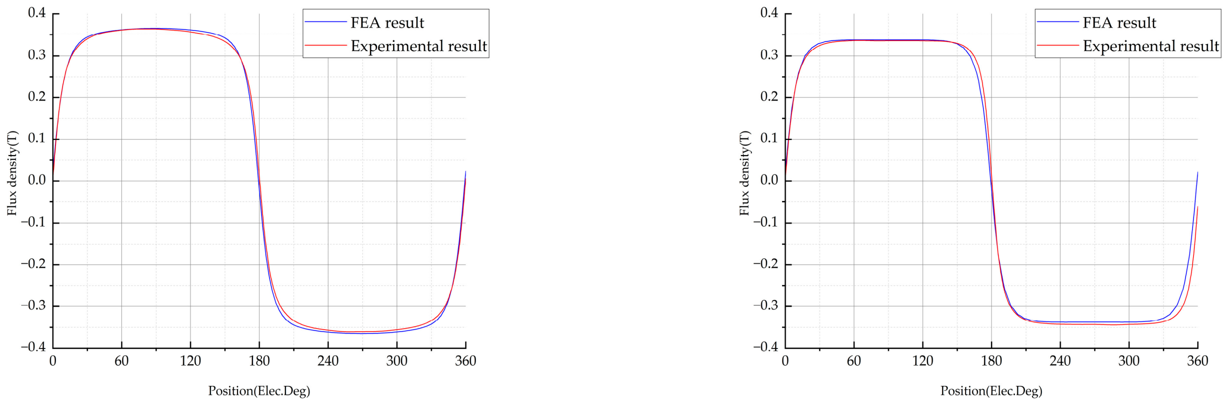

(**a**) (**b**)

Figure 13. Comparison of FEA result and experimental result: (**a**) tile shape PMs; (**b**) PMs under an eccentricity value of 3.5 mm.

Table 2. Comparison of FEA results and experimental results.

Result	λ (mm)	B_{max} (T)	Variation	τ	Variation
FEA Results	Tile PMs	0.3649	-	32.5%	
	3.5	0.3377	-	57.8%	
Experimental Results	Tile PMs	0.3631	−0.48%	29.4%	−9.54%
	3.5	0.3362	−0.44%	56.3%	−2.60%

Analysis of the experimental results showed that the value of τ was 29.4% when the HCM used tile PMs and increased from 29.4% to 56.3% when the HCM used PMs with an eccentricity value of 3.5 mm. The experimental results were in good agreement with the simulation results, proving that the eccentric PM design could effectively improve the proportion of the flat section of the motor AMF and further improve motor performance.

5. Conclusions

For the HCM driven by trapezoidal wave current, the AMF generated by the parallel magnetised PM motor was significantly different from the trapezoidal wave, causing the motor to generate noise or vibration. In this paper, a method for calculating the AMF at any position in the motor was extracted. The partial differential equation between the AMF and the excitation current was constructed using Maxwell's equations, and the PM was equivalent to current in the ESCM, thereby obtaining the AMF distribution. Furthermore, by adjusting the eccentricity value of the PMs, the AMF was improved such that the AMF approached a trapezoidal wave. A prototype HCM was fabricated with different eccentricity values of PMs sintered from high-performance NdFeB material; when the inner diameter of the PMs was eccentric to 3.5 mm, the AMF was closest to the trapezoidal wave, and the proportion of the flat section portion increased from 29.4% to 56.3%. Comparing the analytical result with the FEA result and the experimental result, the width of the flat section of the AMF could be effectively increased, and the trapezoidal characteristic of the AMF of the HCM could be improved, thus reducing the torque ripple of the motor.

Author Contributions: Conceptualisation, J.S. and H.S.; methodology, J.S. and H.S.; validation, J.S., H.S. and X.X.; formal analysis, H.S.; investigation, H.S. and X.X.; resources, H.S. and X.X.; data curation, H.S. and X.X.; writing—original draft preparation, J.S.; writing—review and editing, J.S., H.S. and X.X.; supervision, H.S. and X.X.; project administration, J.S., H.S. and X.X.; funding acquisition, J.S. All authors have read and agreed to the published version of the manuscript.

Funding: This research was funded by the National Nature Science Foundation of China, grant number 52275233.

Institutional Review Board Statement: Not applicable.

Informed Consent Statement: Not applicable.

Data Availability Statement: Not applicable.

Acknowledgments: This research was funded by the National Nature Science Foundation of China, grant number 52275233. The authors would like to thank Gen Xing of the Shanghai Aerospace Control Technology Institute for his contribution to the experimentation and revision of the work.

Conflicts of Interest: The authors declare no conflict of interest.

References

1. Sorokin, A.V.; Yaremenko, V.V. Control Moment Gyroscopes for Spacecraft Attitude Control Systems: History of Development. *Gyroscopy Navig.* **2022**, *13*, 53–58. [CrossRef]
2. Praveen, R.P.; Ravichandran, M.H.; Achari, V.T.S.; Raj, V.P.J.; Madhu, G.; Bindu, G.R. A Novel Slotless Halbach-Array Permanent-Magnet Brushless Dc Motor for Spacecraft Applications. *IEEE Trans. Ind. Electron.* **2012**, *59*, 3553–3560. [CrossRef]
3. Guo, S.; Zhai, C.; Bi, S. Low Voltage Optical Fiber Positioner Robot Based on Minimum Inductance Hollow Cup Motors. *Sci. Rep.* **2022**, *12*, 1–16. [CrossRef] [PubMed]
4. Villani, M.; Tursini, M.; Fabri, G.; Castellini, L. High Reliability Permanent Magnet Brushless Motor Drive for Aircraft Application. *IEEE Trans. Ind. Electron.* **2012**, *59*, 2073–2081. [CrossRef]
5. Liu, J.; Chen, C. Design of Retractile Fins Actuator Based on Hollow Piezoelectric Motor. *J. Phys. Conf. Ser.* **2020**, *1507*, 102008. [CrossRef]
6. Li, E. Research and Design of Four Rotor Aircraft with Wireless Parameter Adjustment Based on Single Chip Microcomputer. *Journal* **2022**, *12257*. [CrossRef]
7. Liu, Z.; Li, S. A Two-Order Active Disturbance Rejection Control Algorithm for Permanent Magnetic Synchronus Motor. In Proceedings of the 2007 Chinese Control Conference, Zhangjiajie, Hunan, China, 26–31 July 2007; Volume 13, pp. 53–58. [CrossRef]
8. Fang, J.; Li, H.; Han, B. Torque Ripple Reduction in Bldc Torque Motor with Nonideal Back Emf. *IEEE Trans. Power Electron.* **2012**, *27*, 4630–4637. [CrossRef]
9. Zhou, X.; Fang, J. Precise Braking Torque Control for Attitude Control Flywheel with Small Inductance Brushless Dc Motor. *IEEE Trans. Power Electron.* **2013**, *28*, 5380–5390. [CrossRef]
10. Zhou, X.; Su, D. Precise Braking Torque Control for Momentum Flywheels Based on a Singular Perturbation Analysis. *J. Power Electron.* **2017**, *17*, 953–962. [CrossRef]
11. Zhou, Y.; Li, H.; Meng, G.; Zhou, S.; Cao, Q. Analytical Calculation of Magnetic Field and Cogging Torque in Surface-Mounted Permanent Magnet Machines Accounting for Any Eccentric Rotor Shape. *IEEE Trans. Ind. Electron.* **2014**, *62*, 3438–3447. [CrossRef]
12. Liu, K.; Rang, Y. Analytical Calculation of Permanent Magnet's Air Gap Magnetic Field of Surface Permanent Magnet Synchronous Mo-Tor. *Ship Electron. Eng.* **2014**, *34*, 147–151. (In Chinese)
13. Ni, Y.Y.; Liu, Y.B. Analytical Calculation of Permanent Magnet Machines with Unequal Thickness Magnets. *Small Spec. Electr. Mach.* **2018**, *46*, 1–5. (In Chinese) [CrossRef]
14. Kang, G.H.; Hur, J.; Kim, W.B.; Lee, B.K. The Shape Design of Interior Type Permanent Magnet Bldc Motor for Minimization of Mechanical Vibration. In Proceedings of the 2009 IEEE Energy Conversion Congress and Exposition, San Jose, CA, USA, 20–24 September 2009. [CrossRef]
15. Prashanth, N.A. Flux Maximization in Wind Turbine Permanent Magnet Synchronous Generator Made of Ndfeb Permanent Magnets. *Mater. Today Proc.* **2022**, *49*, 731–737. [CrossRef]
16. Peng, P.; Zhang, J.; Li, W.; Leonardi, F.; Rong, C.; Degner, M.W.; Liang, F.; Zhu, L. Time-Dependent Demagnetisation of Ndfeb Magnets under Dc and Pulsed Magnetic Fields. *IEEE Trans. Magn.* **2020**, *56*, 6100310. [CrossRef]
17. Zhou, T.J.; Hu, X.J.; Pan, W.M.; Xie, W.C.; Zeng, Q.W.; Liu, R.H.; Li, M.F.; Du, J.F.; Zhong, Z.C. Influencing Factors on Flux Irreversible Loss of Nd-Fe-B Magnet Application. *J. Chin. Soc. Rare Earths* **2019**, *37*, 339–343. (In Chinese)
18. Cao, Y.; Liu, Y.; Zhang, P.; Xu, G.; Liu, J.; Chen, J.; Yi, X.; Wu, Y. Corrosion Resistance and Mechanical Properties of (Ho, Nd)Feb Magnets. *J. Rare Earths* **2021**, *39*, 1409–1414. [CrossRef]
19. Kim, T.-H.; Lee, S.-R.; Bae, K.-H.; Kim, H.-J.; Lee, M.-W.; Jang, T.-S. Effects of Al/Cu Co-Doping on Crystal Structure and Chemical Composition of Nd-Rich Phases in Nd-Fe-B Sintered Magnet. *Acta Mater.* **2017**, *133*, 200–207. [CrossRef]
20. Fu, S.; Liu, X.; Jin, J.; Zhang, Z.; Liu, Y.; Yan, M. Magnetic Properties Evolution with Grain Boundary Phase Transformation and Their Growth in Nd-Fe-Cu-Ga-B Sintered Magnet During Post-Sinter Annealing Process. *Intermetallics* **2021**, *137*, 107303. [CrossRef]
21. Huang, Q.; Jiang, Q.; Shi, Y.; Rehman, S.U.; Wei, X.; Li, Z.; Shi, D.; Xu, D.; Zhong, Z. Enormous Improvement of the Coercivity of Ga and Cu Co-Doping Nd-Fe-B Sintered Magnet by Post-Sinter Annealing. *J. Alloys Compd.* **2022**, *894*, 162418. [CrossRef]
22. Wang, F.; Chen, K.; Du, J.; Zhang, J. Simultaneous Increase in Remanence and Coercivity during Grain Refining of Nd-Fe-B Deformed Magnets. *J. Rare Earths* **2022**, *40*, 1763–1771. [CrossRef]
23. Zhu, X. New Technology of Making Ndfeb by Sintering. *Insight—Mater. Sci.* **2018**, *1*, 9–16. [CrossRef]

24. Durán Perdomo, J.F.; Pérez Alcázar, G.A.; Colorado, H.D.; Tabares, J.A.; Zamora, L.E.; Garitaonandia, J.J.S. Systematic Study of the Dependence of Magnetic and Structural Properties of Nd2fe14b Powders on the Average Particle Size. *J. Rare Earths* **2020**, *38*, 961–968. [CrossRef]
25. Sun, J.; Ren, J.; Sun, H. A Novel Design of an Inner Rotor for Optimising the Air-Gap Magnetic Field of Hollow-Cup Motors. *Machines* **2022**, *10*, 314. [CrossRef]
26. Sun, J.; Ren, J.; Le, Y.; Wang, H. Analysis of Air-Gap Magnetic Field and Structure Optimization Design of Hollow-Cup Motor. *Aerospace* **2022**, *9*, 549. [CrossRef]